Journal of Materials Chemistry B

ROYAL SOCIETY OF CHEMISTRY

PAPER

View Article Online
View Journal | View Issue

Cite this: J. Mater. Chem. B, 2024, 12, 1379

pH-Responsive nanoplatform synergistic gas/photothermal therapy to eliminate biofilms in poly(L-lactic acid) scaffolds

Guowen Qian, *[ab] Yuqian Mao,[a] Huihui Zhao,[a] Lemin Zhang,[a] Long Xiong[c] and Zhisheng Long*[b]

To date, implant-associated infection is still a significant clinical challenge, which cannot be effectively eliminated by single therapies due to the formation of microbial biofilms. Herein, a pH-responsive nanoplatform was constructed *via* the *in situ* growth of zinc sulfide (ZnS) nanoparticles on the surface of Ti_3C_2 MXene nanosheets, which was subsequently introduced in poly(L-lactic acid) (PLLA) to prepare a composite bone scaffold *via* selective laser sintering technology. In the acidic biofilm microenvironment, the degradation of ZnS released hydrogen sulfide (H_2S) gas to eliminate the biofilm extracellular DNA (eDNA), thus destroying the compactness of the biofilm. Then, the bacterial biofilm became sensitive to hyperthermia, which could be further destroyed under near-infrared light irradiation due to the excellent photothermal property of MXene, finally achieving gas/photothermal synergistic antibiofilm and efficient sterilization. The results showed that the synergistic gas/photothermal therapy for the composite scaffold not only evidently inhibited the formation of biofilms, but also effectively eradicated the eDNA of the already-formed biofilms and killed 90.4% of *E. coli* and 84.2% of *S. aureus* under near infrared light irradiation compared with single gas or photothermal therapy. In addition, the composite scaffold promoted the proliferation and osteogenic differentiation of mouse bone marrow mesenchymal stem cells. Thus, the designed scaffold with excellent biofilm elimination and osteogenesis ability has great potential as an alternative treatment for implant-associated bone infections.

Received 2nd November 2023,
Accepted 4th January 2024

DOI: 10.1039/d3tb02600k

rsc.li/materials-b

1. Introduction

Implant-associated infections (IAIs) caused by bacterial colonization are a common cause of orthopedic graft failure. In this case, antibiotics are currently used to treat IAIs in the clinic.[1,2] However, multidrug-resistant strains are emerging and becoming prevalent due to the abuse of antibiotics.[3,4] Accordingly, researchers have attempted to add inorganic antibacterial agents such as the heavy metals copper and silver and their composites to scaffolds as an alternative to antibiotics, given that their unique physicochemical properties endow them with excellent antibacterial properties.[5,6] However, their potential toxicity and instability are still significant concerns.[7,8] Therefore, there is an urgent need to seek safe, effective, and drug-free antibacterial methods.

Recently, photothermal therapy (PTT) has gained widespread attention and is considered to be a suitable option due to its operability, controllability, and biosafety.[9] However, clinically, most bacteria tend to adhere irreversibly to the implant surface and form extracellular polymeric substances (EPS), which are also called biofilms.[10–13] In this case, once a bacterial biofilm is formed, PTT will encounter significant obstacles. Alternatively, as an emerging field, gas therapy has attracted increasing attention as a green therapy in the treatment of bacterial infections.[14] Furthermore, gas therapy is often combined with other treatments to achieve bacterial eradication. Hydrogen sulfide (H_2S), the third gas signal molecule after carbon monoxide (CO) and nitric oxide (NO), combines the advantages of NO and CO and plays an important role in the treatment of some diseases.[15] For instance, Fu *et al.*[16] found that exogenous H_2S can promote the production of reactive oxygen species (ROS) in bacteria, which will lead to lipid peroxidation and DNA damage. Li *et al.*[17] reported that H_2S gas can inhibit mitochondrial respiration and ATP synthesis, thus inducing apoptosis in cancer cells. Therefore, we hypothesize that combining photothermal therapy with H_2S gas therapy will be promising for combating refractory IAIs.

[a] School of Energy and Mechanical Engineering, Jiangxi University of Science and Technology, Nanchang 330013, P. R. China. E-mail: qianguowen@jxust.edu.cn
[b] Department of Orthopedics, Jiangxi Provincial People's Hospital, The First Affiliated Hospital of Nanchang Medical College, Nanchang 330006, P. R. China. E-mail: ffyhve@163.com
[c] Department of Orthopedics, The Second Affiliated Hospital of Nanchang University, Nanchang, 330008, P. R. China

As a common donor of H_2S, zinc sulfide (ZnS) can release H_2S gas in the acidic microenvironment of biofilms, thus enabling the precise release of H_2S gas.[18] However, its wide band gap (3.6 eV) prevents it from effectively absorbing NIR light, and thus it cannot be used as a photothermal material for biomedical applications.[19] As an emerging two-dimensional nanomaterial, Ti_3C_2 MXene has attracted extensive attention due to its good biocompatibility, large specific surface area and excellent light absorption properties.[20,21] Moreover, due to its strong localized surface plasmon resonance (LSPR) effect, monolayer Ti_3C_2 MXene exhibits excellent photothermal properties.[22,23] Therefore, it can compensate for the low near-infrared (NIR) light absorption of ZnS nanoparticles. Based on the above-mentioned facts, we hypothesized that a nanoplatform constructed by the *in situ* growth of ZnS on the surface of Ti_3C will exhibit efficient biofilm elimination and antibacterial activity under NIR light irradiation.

Over the past few years, numerous synergistic strategies have been reported for disease treatment.[24–26] For example, Ou *et al.*[27] constructed black phosphorus nanosheet (BPNS)-functionalized Chl cells (Chl@BP-Fe), synchronously ameliorating tumor hypoxia and realizing synergistic photodynamic/chemodynamic/immune therapy. Lin *et al.*[28] constructed a calcium sulfide (CaS)-based nanoregulator (I-CaS@PP) to enhance H_2S-boosted Ca^{2+}-mediated tumor-specific therapy, which significantly inhibited tumor thermal resistance to achieve synergistic therapy. Yu *et al.*[29] enhanced the antitumor effect by developing oxidative stress-amplifying nanomedicine (p53/Ce6@ZF-T), which amplified intratumoral oxidative stress through chemical kinetic/photodynamic synergy. Compared with these synergistic strategies for disease treatment, the ZT nanoplatform could realize the release of H_2S gas in the acidic microenvironment of the biofilm, which prevented the damage from H_2S gas to normal tissues. In addition, the heat resistance of the bacteria was reduced due to the damage by H_2S to the biofilm, which could kill bacteria at relatively mild temperatures. More importantly, the damage of the mild photothermal effect to normal tissues was significantly low.

In this work, as shown in Scheme 1, we report the preparation of a pH-responsive ZnS–Ti_3C_2 nanoplatform *via* the *in situ* growth of ZnS on the surface of Ti_3C_2 to resist bacterial biofilm infection, which was subsequently incorporated in PLLA to fabricate composite scaffolds employing selective laser sintering (SLS) technology.[30,31] In the normal physiological environment, ZnS–Ti_3C_2 remained stable. Once biofilm infection occurred on the implant, the nanoplatform in the composite scaffold could respond to the acidic pH microenvironment of the biofilms and release H_2S gas for precise gas treatment to disrupt the extracellular DNA (eDNA) in the biofilms. Under NIR irradiation, the composite scaffolds with ZnS–Ti_3C_2 could produce hyperthermia, efficiently killing the biofilm-damaging bacteria at a relatively mild temperature. Another advantage of this composite scaffold is that the Zn^{2+} generated by the degradation of the scaffold could significantly promote osteogenic differentiation.[32,33]

2. Materials and methods

2.1. Materials

Zinc acetate ($Zn(CH_3CO_2)_2$) and thiourea (CH_4N_2S) were purchased from Aladin Biochemical Technology Co. Ltd. Ti_3AlC_2 was purchase from Jilin 11 Technology Co., Ltd. Lithium fluoride (LiF), hydrochloric acid (HCl) and polyvinylpyrrolidone (PVP) were purchased from Macklin Co. Ltd. PLLA (M_w = 150 kDa) powder was purchased from Shenzhen Polymtek Biomaterial Co., Ltd.

2.2. Synthesis of monolayer Ti_3C_2

According to previous studies, Ti_3C_2 can be prepared by chemical stripping of the Al phase of Ti_3AlC_2.[34,35] Firstly, 1 g of LiF was slowly added to 20 mL of hydrochloric acid (9 mol L^{-1}) and stirred for 20 min for total dissolution, and the final mixed solution was labeled as solution A. Then, 1 g of Ti_3AlC_2 powder was carefully added to solution A and stirred at 35 °C for 48 h. The obtained solid was washed by centrifugation with deionized water at 3500 rpm 5–7 times until the pH of the supernatant

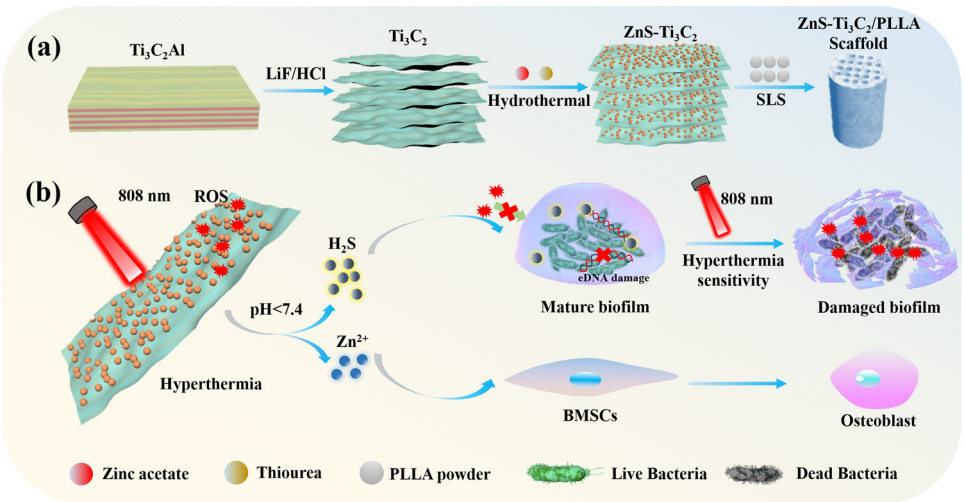

Scheme 1 (a) Schematic diagram of the preparation of the multifunctional scaffold. (b) Antimicrobial and mechanism of bone differentiation.

reached 6, and finally the multilayer Ti_3C_2 was successfully obtained. To prepare monolayer Ti_3C_2 nanosheets, the final multilayer Ti_3C_2 was lyophilized and the lyophilized product was dispersed in 40 mL of deionized water, sonicated and stirred under a nitrogen atmosphere for 30 min, followed by centrifugation at 3500 rpm for 60 min, and the supernatant was collected and stored at 4 °C.

2.3. Preparation of ZnS and ZnS–Ti_3C_2

ZnS nanoparticles were synthesized *via* the typical hydrothermal method. Firstly, $[Zn(CH_3COO)_2]\cdot 2H_2O$ (1.0 g) was dissolved in 40 mL ethylene glycol solution, and then 0.5 g of thiourea was added and stirred continuously for 20 min. Subsequently, the mixture was transferred to a 100 mL Teflon-coated stainless steel autoclave and heated at 140 °C for 10 h. After cooling naturally to room temperature, the product was washed with DI water and dried at 60 °C overnight to obtain ZnS nanoparticles.

The ZnS–Ti_3C_2 (ZT) nanoplatform was prepared *via* the *in situ* hydrothermal growth of ZnS nanoparticles on the surface of Ti_3C_2. Firstly, 0.1 g monolayer Ti_3C_2 nanosheets was dissolved in 20 mL DI water and sonicated for 10 min. Afterwards, 1.6 g of $[Zn(CH_3COO)_2]\cdot 2H_2O$ and 0.8 g of thiourea were added to the above-mentioned solution and stirred for 30 min, and then the solution was transferred to a Teflon-coated stainless steel autoclave and heated at 140 °C for 12 h. Finally, the ZT nanoplatform was obtained after washing, centrifuging and drying.

2.4. Physicochemical characterization

The surface micromorphology and detailed microstructure of the prepared powders were observed by scanning electron microscopy (SEM, EVO18, ZEISS, Germany) and transmission electron microscopy (TEM, JEOL, 2100F, Japan), respectively. The distribution of Zn, Ti, S and C elements in the ZT powder was analyzed by energy dispersion spectroscopy (EDS, Bruker, Germany). The crystal structures of the prepared powders were characterized by X-ray diffraction (XRD, D8 Advance, Bruker Co, Germany). The elemental composition, atomic valence and molecular structure of the powders were analyzed by X-ray photoelectron spectroscopy (XPS, Thermo, USA). In addition, the thermal behavior of the powders was detected by thermogravimetric analysis (TGA, WTC-122, China).

2.5. Preparation and characterization of bone scaffolds

The composite powders were prepared by grinding ZT nanoparticles with PLLA powder in the mass ratio of 4 : 96 for 30 min, and then the composite powders were added to absolute ethanol under ultrasonic stirring for 2 h. After filtering and vacuum drying, the composite powders were used to fabricate composite bone scaffolds by selective laser sintering (SLS) technology.[36–38] Before sintering, a pre-design 3D scaffold model was imported into the SLS system, and then the model was sliced and layered. The sintering forming process is described as follows: (1) a layer of composite powder was spread evenly on the surface of the plate, and the SLS system controlled the laser to scan over the composite powder layer according to the preset contour. (2) When the temperature increased to the melting point, the powder melted and bonded with the molded part below. (3) After one layer was completed, the table dropped one layer in thickness and the spreading roller continued to spread a layer of powder on the top, and the laser continued to scan the powder layer on a prescribed path until the whole model was finished. (4) Finally, the ZT/PLLA scaffolds were obtained after removing the excess powder. The printing parameters during the sintering progress were set as follows: scanning speed of 150 mm s^{-1}, layer thickness of 0.1 mm and laser power of 2 W. In addition, the process for the preparation of the PLLA, ZnS/PLLA and Ti_3C_2/PLLA scaffolds was the same as that for the ZT/PLLA scaffold.

The surface morphologies of the scaffolds were detected by scanning electron microscopy (SEM, Zeiss, Germany) equipped with EDS (Bruker, Germany). Besides, the scaffolds were analyzed using a surface contact angle analyzer (DSA-Alpha, China).

2.6. Photothermal effect of the scaffolds

To evaluate the photothermal properties of the different groups of scaffolds, the PLLA, ZnS/PLLA, Ti_3C_2/PLLA and ZT/PLLA scaffolds were placed in EP tubes containing 7 mL of phosphate buffered saline (PBS, pH = 7.4) and irradiated with an 808 nm NIR laser at a power density of 1.0 W cm^{-2}. The heating curves and photothermal images at different moments were recorded using a multichannel temperature recorder (MT-8X, Shenhuwa, Shenzhen) and infrared thermography imager (E50, FLIR, USA), respectively. In addition, to evaluate the photothermal stability and photothermal conversion efficiency of the ZT/PLLA scaffold, it was irradiated for 10 min, and then naturally cooled to room temperature, and the heating–cooling cycle was repeated five times to record the cycle curve and the heating–cooling curve, which were used to characterize the photothermal stability and the photothermal conversion efficiency of the ZT/PLLA scaffold, respectively, where the photothermal conversion efficiency was calculated using the equation developed by Roper *et al.*[39]

2.7. H_2S generation and Zn^{2+} release by the ZT/PLLA scaffold

To detect the generation of H_2S, the methylene blue colorimetry method was performed. Briefly, the ZT/PLLA scaffolds were immersed in 10 mL of phosphate buffered saline (PBS; pH = 7.4, 6.2, 5.0) under constant shaking at 37 °C. At preset times (0, 1, 2, 4, 8, 16, and 24 h), 1 mL of PBS was withdrawn and mixed with 1 mL mixed solution of zinc acetate (4 mg mL^{-1}) and sodium acetate (1 mg mL^{-1}). The precipitate was collected after centrifuging at 10 000 rpm for 30 min and re-dissolved in 500 μL mixed solution containing *N*,*N*-dimethyl-*p*-phenylenediamine sulfate (1.4 mg mL^{-1}) and $FeCl_3$ (5 mg mL^{-1}). After incubation at 37 °C for 20 min, methylene blue was formed and measured using a microplate reader (Varioskan LUX, Thermo Scientific, USA) at the absorbance of 664 nm. To quantify the concentration of H_2S at each time point, a standard curve was created using sodium sulfide (Na_2S).

In the case of the Zn^{2+} release experiments, the ZT/PLLA scaffolds were soaked in PBS under constant shaking at 37 °C.

The solution was changed with fresh PBS at preset times (1, 3, 5, 7, 10, and 14 days), and the liquid was collected and refrigerated. Finally, the concentration of Zn^{2+} in the liquid was detected using an inductively coupled plasma atomic emission spectrometer (ICP-AES, Optima 5300 DV, PerkinElmer, USA).

2.8. Antibacterial assays

2.8.1. *In vitro* anti-biofilm performance. *Escherichia coli* (*E. coli*, ATCC 25922) and *Staphylococcus aureus* (*S. aureus*, ATCC 25923) were chosen as the two model bacteria to evaluate the therapeutic effect of different treatments on biofilms. Briefly, the bacteria at a density of 10^7 CFU mL^{-1} were seeded on the scaffolds for 48 h at 37 °C to form biofilms. After that, the biofilms were treated with NIR light for 20 min or in the dark, and the remaining biofilm was fixed with methanol solution and stained with crystal violet, and the stained images were taken using a digital camera. For the quantitative analysis of the biofilms, the residual dye was washed with glacial acetic acid, and the eluates were measured on a microplate reader (Varioskan LUX, Thermo) at 570 nm. According to the spread plate method (SPM), the bacterial and biofilm solution was diluted by 1×10^4 times and 100 μL of the solution was withdrawn and spread evenly on agar plates. After incubation at 37 °C for 24 h, pictures of the *E. coli* and *S. aureus* plates were captured using a digital camera, and the bacterial colonies on the plates were counted using the ImageJ software.

2.8.2. Bacterial biofilm morphology. *E. coli* biofilms were established according to previous study. The scaffolds were placed in 48-well and incubated with bacterial solution (1×10^7 CFU mL^{-1}) at 37 °C for 48 h. Then, the biofilm-scaffold constructs were treated with NIR light for 20 min or in the dark. After fixing the biofilm with 2.5% glutaraldehyde at 37 °C for 30 min, graded ethanol (30%, 50%, 75%, 80%, 85%, 90%, 95% and 100%) was used to dehydrate the biofilms. After drying at 37 °C, the biofilm-scaffold constructs were sputtered with platinum and observed on an SEM (EVO 18, Zeiss, Germany).

2.8.3. DAPI/PI staining assay. To further investigate the antibacterial activity of the ZT/PLLA scaffold, dihydrochloride (DAPI)/propidium iodide (PI) was used to stain the bacteria. DAPI can stain all live and dead bacteria, while PI can only stain bacteria with damaged cell membranes. After the scaffolds were co-cultured with bacteria for 12 h, NIR light was applied to irradiate the scaffold for 20 min. Then, the bacteria were stained with DAPI/PI staining kits for 30 min and washed with PBS twice. Afterwards, a fluorescence microscope (CKX53, OLYMPUS) was used to capture the fluorescence images of the bacteria.

2.8.4. gDNA level and eDNA staining assays. The genomic DNA (gDNA) of *E. coli* and *S. aureus* was extracted using a bacterial DNA extraction kit (Solarbio, Beijing). The extracted gDNA was dispersed in DNase- and RNase-free water. After treating the gDNA solution with PLLA, ZnS/PLLA, Ti_3C_2/PLLA and ZT/PLLA for 12 h, each group of gDNA was collected by centrifugation. Then, 1% agarose gel electrophoresis was employed to analyze the gDNA cleavage products. Besides, the concentration of gDNA was determined using an ultramicro-spectrophotometer (B-500, Metash, Shanghai).

An acridine orange (AO) staining kit (Beyotime, Shanghai, China) was applied for the assessment of the destruction of the biofilm eDNA. Briefly, after different treatments, the bacteria-scaffold constructs were taken out and rinsed twice with PBS, and then the eDNA of the biofilms was stained by AO dye for 30 min. Finally, the staining results were observed by a fluorescence microscope to detect the biofilm eDNA damage on the scaffolds.

2.8.5. ONPG hydrolysis assay. The differently treated biofilms were collected by shaking and ultrasonication. The collected biofilm suspension was mixed with *O*-nitrophenyl-β-galactoside (ONPG) solution and incubated at 37 °C. ONPG will hydrolyze to *o*-nitrophenol (ONP) during the reaction with β-D-galactosidase, which appears yellow under alkaline conditions. Then, the absorbance of the mixture was recorded using a microplate reader (Varioskan LUX, Thermo) at 420 nm.

2.9. Cell behaviors

2.9.1. Cell proliferation. Mouse bone marrow mesenchymal stem cells (mBMSCs, ATCC) were used for cell experiments. Before the experiment, the scaffolds (Φ 8 mm × 1.5 mm) were sterilized by immersion in 75% ethanol for 4 h, and then exposure to UV light for 4 h. To evaluate the cytocompatibility and proliferation of the cells under different culture conditions, a counting kit-8 (CCK-8) experiment was performed. Firstly, the different scaffolds were soaked in the medium for 24 h and the extraction solution collected, where the weight-to-volume ratio of the scaffold in the culture medium was 25 mg mL^{-1}. The cells at a density of 3×10^3 cells per well were seeded on a 96-well plate, and the medium was changed with the extraction solution every other day. After culturing for 1, 3 and 5 days, the medium was replaced with the CCK8 solution and incubated at 37 °C for 1 h. Then, the optical density was measured using a microplate reader (Varioskan LUX, Thermo) at 450 nm. Subsequently, the cells were stained using calcein-AM/PI (Beyotime, Shanghai, China) for 30 min and observed under a fluorescence microscope (BX51 Olympus, Japan).

2.9.2. ALP and alizarin red staining assays. The alkaline phosphatase (ALP) activity of the mBMSCs on the scaffolds was assessed. Firstly, the different scaffolds were soaked in the medium for 24 h and the extraction solution collected, where the weight-to-volume ratio of the scaffold in the culture medium was 25 mg mL^{-1}, and then osteogenic induction solution with 0.1 μM dexamethasone, 50 mM ascorbic acid and 10 mM sodium β-glycerophosphoric acid was added. The cells were seeded at a density of 1×10^4 cells per well on a 48-well plate. The culture medium was changed with the extract solution every other day. After 7 days of incubation, the cells were fixed with 4% paraformaldehyde for 30 min, and then washed with PBS three times. Finally, the cells were stained using alkaline phosphatase (Beyotime, Shanghai, China) and Alizarin red staining kits (Solarbio, Beijing, China), and the staining results were observed under a fluorescence microscope.

2.10. Statistic analysis

All experimental data were obtained from at least three independent experiments and the data expressed as mean ± SD.

Statistical analysis of all data was carried out using Origin 2021. The differences between two groups of different results were analyzed by Student's t test and considered significantly different when $^{*}p < 0.05$, $^{**}p < 0.01$, and $^{***}p < 0.001$.

3. Results and discussion

3.1. Synthesis and characterizations of ZnS, Ti_3C_2 and ZT

The scanning electron microscopy (SEM) image of the Ti_3C_2 particles displayed an accordion-like layered structure (Fig. 1a). This was due to the loss of the Al layer in the Ti_3AlC_2 precursor.[40] The SEM image of the ZnS particles showed that the ZnS nanoparticles exhibited a regular spherical morphology with an average particle size of 40–50 nm and agglomerated (Fig. 1b). By comparison, the SEM image of the ZT nanoplatform exhibited that the ZnS nanoparticles adhered uniformly to the surface of the Ti_3C_2 nanosheets without agglomeration (Fig. 1c). Furthermore, the transmission electron microscopy (TEM) image of ZT indicated that the ZnS nanoparticles were tightly bonded to the Ti_3C_2 nanosheets (Fig. 1d). Fig. 1e–i demonstrate the bright-field images and corresponding element mapping images, confirming the existence of Zn, S, Ti, C elements and their uniform dispersion on the surface of the ZT nanoplatform, respectively. Besides, high-resolution transmission electron microscopy (HR-TEM) characterization was performed. As shown in Fig. 1j and k, the lattice spacing of 0.26 nm represents the (0110) plane of Ti_3C_2 and 0.31 nm denotes the (103) plane of ZnS. This is direct evidence for the successful combination of ZnS and Ti_3C_2 to form the ZT nanoplatform. The selected area electron diffraction (SAED) pattern of ZT showed diffraction rings associated with the (103), (1011), and (204) planes of wurtzite ZnS (ICDD card no. 04-008-7254) (Fig. 1l).

X-ray powder diffraction (XRD) was carried out to characterize the phase and crystallinity of the powders. Fig. 2a shows the XRD pattern of Ti_3C_2, ZnS, and ZT. The peak signals of the Ti_3AlC_2 precursors at the 2θ values of 38.9° and 56.8° almost disappeared in the pattern of Ti_3C_2. In addition, the peak at $2\theta \approx 9.4°$ was shifted to $2\theta \approx 6.2°$ due to the etching effect. All these results confirmed the successful etching of Ti_3AlC_2. In the spectrum of the pure ZnS, the diffraction peaks at $2\theta \approx 29°$, 48.6°, and 57.2° correspond to the (103), (1011), and (204) planes of wurtzite ZnS (ICDD card no. 04-008-7254), respectively, which are consistent with the data in the previous section from SEAD mapping. The distinct ZnS diffraction peaks were observed in the XRD spectrum of ZT without any shift, indicating that the hybridization of ZnS and Ti_3C_2 did not affect their crystalline properties. In addition, in the XRD spectrum of ZT, the diffraction peaks at $2\theta \approx 6.2°$ and 60.6° correspond to the (002) and (110) planes of Ti_3C_2, respectively, which further demonstrated that ZnS was successfully grown on the surface of Ti_3C_2. However, not all the peaks of Ti_3C_2 were observed in the XRD spectrum of ZT. This is due to the relatively low content of Ti_3C_2 in ZT, which resulted in the characteristic crystal planes being covered by the diffraction peaks of ZnS.

Fig. 2b displays the full XPS survey spectra of the samples, where the peaks for Zn 2p, S 2p, Ti 2p and C 1s were detected in

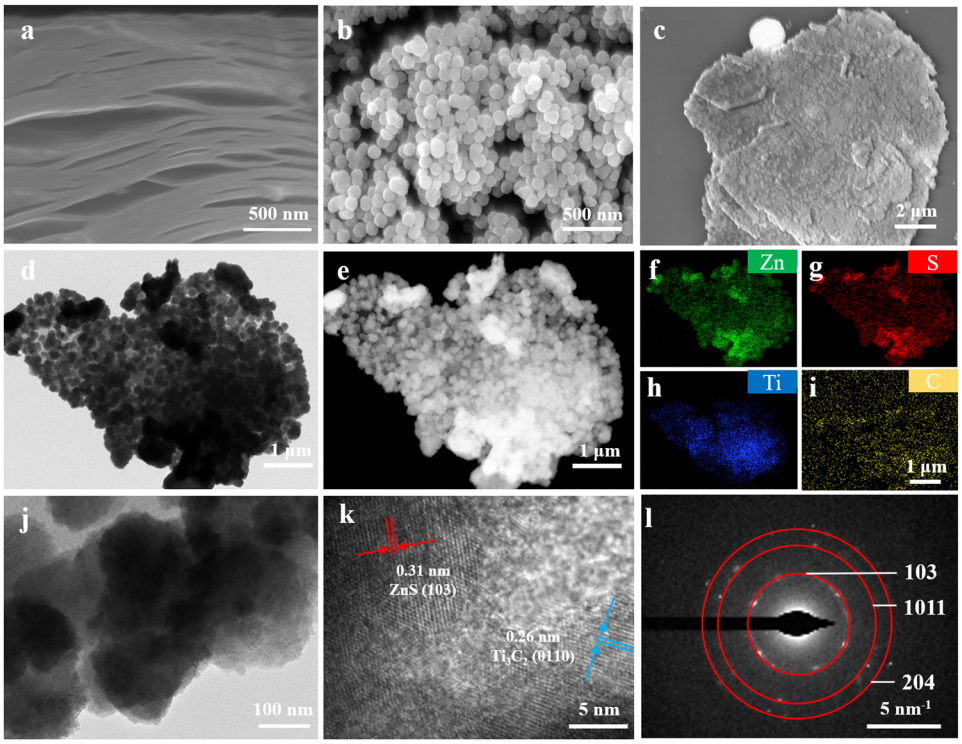

Fig. 1 SEM images of Ti_3C_2 (a), ZnS (b) and ZT (c). (d) Low-resolution TEM image of ZT. Dark-field (e) and element mapping (f)–(i) of ZT. TEM (j), high-resolution TEM (k) and SAED (l) images of ZT nanoplatform.

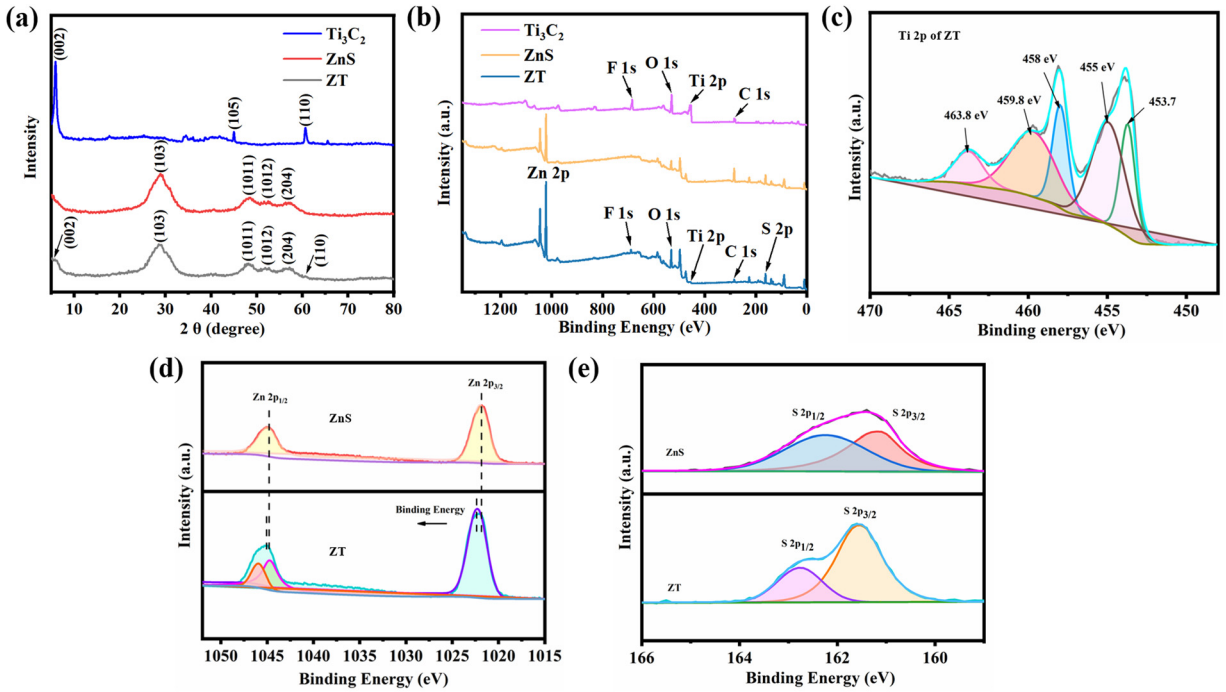

Fig. 2 XRD (a) and full XPS survey (b) spectra of ZnS, Ti_3C_2 and ZT nanoparticles. (c) High-resolution Ti 2p XPS spectra of ZT. (d) High-resolution Zn 2p XPS spectra of ZnS and ZT. (e) High-resolution S 2p XPS spectra of ZnS and ZT.

the XPS spectrum of ZT, indicating that the ZT nanoplatform was constructed successfully. The Ti 2p spectrum of ZT, as shown in Fig. 2c, showed signals located at the binding energies of 453.7, 455, 458, 459.8 and 463.8 eV, which can be attributed to Ti(III) $2p_{3/2}$, Ti(II) $2p_{3/2}$, Ti(IV) $2p_{3/2}$, Ti(II) $2p_{1/2}$, and Ti(IV) $2p_{1/2}$, respectively. The high-resolution Zn 2p spectra of pure ZnS and ZT are shown in Fig. 2d, where it can be observed that the binding energies of Zn $2p_{3/2}$ and Zn $2p_{1/2}$ appeared at about 1022.0 eV and 1045.3 eV in the XPS spectrum of pure ZnS. After the nanoplatform was formed, the Zn $2p_{1/2}$ and Zn $2p_{3/2}$ peaks shifted to slightly higher binding energies. The same trend was observed in the high-resolution spectrum of S 2p. Besides, the high-resolution spectrum of S 2p showed two peaks at 161.8 eV and 162.9 eV, indicating that S element existed in the form of S^{2-}.[41] All these results indicate the strong interface bonding between ZnS and Ti_3C_2.

3.2. Synthesis and characterization of composite scaffolds

It is desirable for an ideal scaffold to possess an interconnected porous structure to match the structural properties of natural bone and facilitate the transport of nutrients.[42,43] Selective laser sintering technology (SLS) has a wide range of applications in the porous structure and personalization of bone scaffolds due to its rapidity and high precision, allowing precise control of the pore distribution, pore size and number to meet the needs of different types of bone repair.[44–46] The digital images of the sintered scaffolds are shown in Fig. 3a. It can be seen that the prepared scaffolds were cylinder-shaped and possessed an interconnected porous structure with a pore size of ~400 μm.

The comprehensive performance of the composite scaffolds mainly depends on the dispersion state of the nanofillers in the matrix. Thus, to observe the distribution state of the nanofillers in the matrix, SEM and EDS elemental mapping was carried to analyze the surface microstructure and compositions of the composite scaffolds (Fig. 3b–e). It was observed that the ZT nanoparticles were uniformly embedded in the PLLA matrix. There were no cracks and pores on the surface of the scaffold, indicating the good sintering performance of the ZT/PLLA scaffold. In addition, based on the thermogravimetric analysis (TGA) curves of Ti_3C_2, ZnS and ZT, as shown in Fig. 3f, it can be concluded that the contents of ZnS and Ti_3C_2 in the ZT/PLLA scaffolds were 2.15% and 1.85%, respectively. Besides, the water contact angle (WCA) of the composite scaffolds was also measured. As shown in Fig. 3g, the addition of ZnS, Ti_3C_2 and ZT increased the hydrophilicity of the scaffolds. Excellent hydrophilicity facilitates the absorption of nutrients and proteins, thereby promoting the adhesion and proliferation of cells.[47]

The ZT nanoplatform is expected to have excellent photothermal property when irradiated by NIR light, given that Ti_3C_2 is a well-known photothermal material. The photothermal images of the scaffolds after irradiation for different times under 808 nm NIR laser are displayed in Fig. 4a. The PLLA scaffold showed a negligible photothermal effect, and the introduction of ZnS did not significantly improve its photothermal properties due to its poor NIR light absorption. By contrast, the temperature of the Ti_3C_2/PLLA and ZT/PLLA scaffolds increased rapidly with an extension of the irradiation time. The variation in temperature for the different scaffolds after irradiation for different times is exhibited in Fig. 4b.

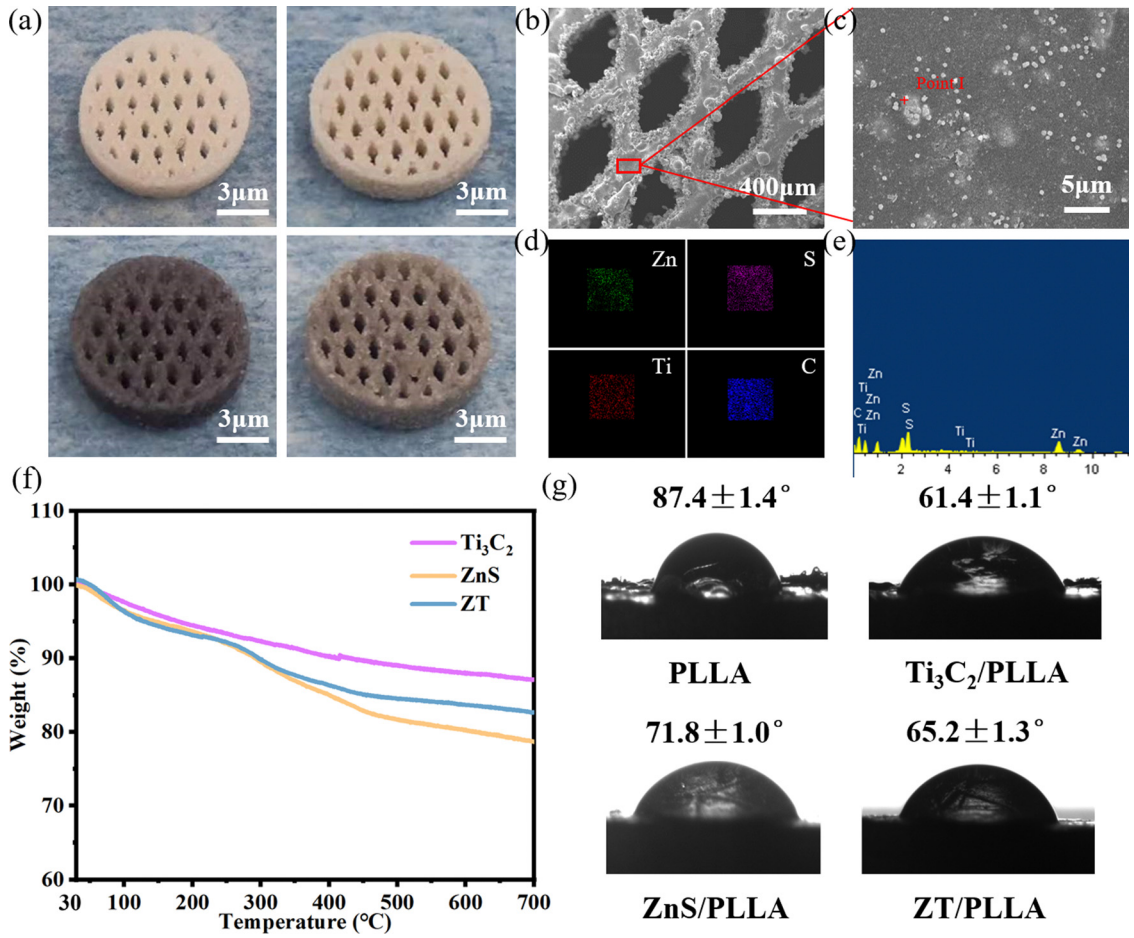

Fig. 3 (a) Digital images of the prepared scaffolds. (b) and (c) Surface microstructure of the ZT/PLLA scaffold. (d) Mapping images of red rectangular box in (b). (e) EDS spectra in point I. (f) TGA curves of Ti_3C_2, ZnS, and ZT. (g) Water contact angles of the composite scaffolds.

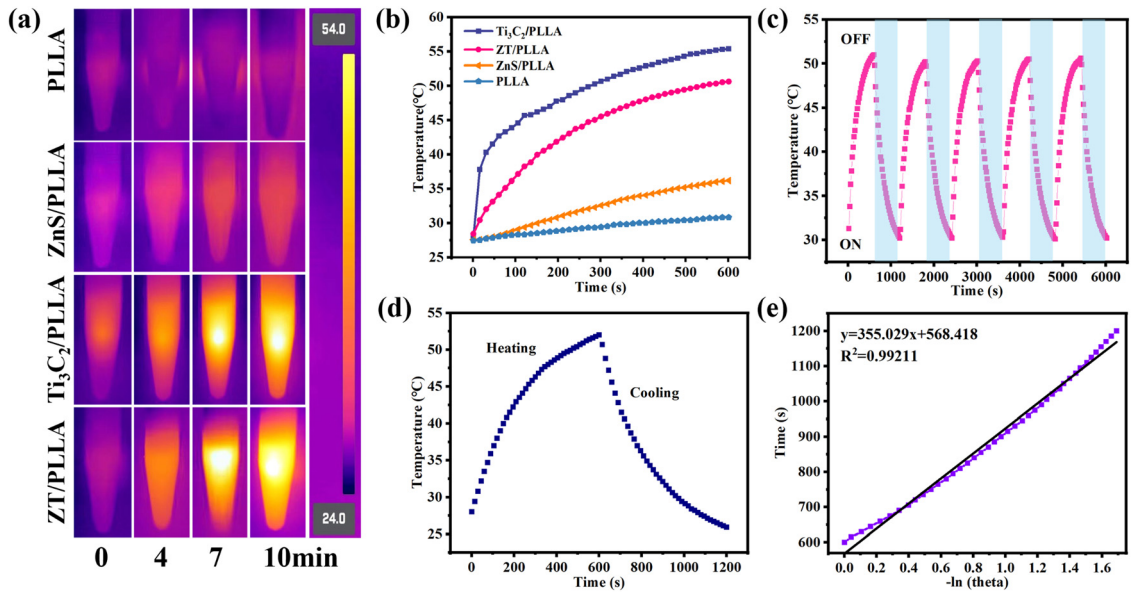

Fig. 4 Photothermal images (a) and curves (b) of the composite scaffolds under NIR light for different irradiation times. (c) Thermal cycle curves of the ZT/PLLA scaffold. (d) Single temperature rising and cooling curve of the ZT/PLLA scaffold. (e) Regression curve of the ZT/PLLA scaffold cooling period.

The temperature for the PLLA scaffold only increased from 27.0 °C to 31.1 °C under irradiation from NIR light for 10 min. The addition of ZnS particles slightly increased the photothermal properties, where the temperature of the ZnS/PLLA scaffold increased from 26.3 °C to 36.0 °C after irradiation from NIR light for 10 min. By contrast, the temperature of the Ti_3C_2/PLLA and ZT/PLLA scaffolds reached to 55.2 °C and 51 °C under irradiation from NIR light for 10 min, respectively. In addition, the photothermal stability of the scaffolds was also evaluated (Fig. 4c). There were no obvious changes in the temperature range when NIR light was applied to the ZT/PLLA scaffold for 5 cycles, indicating its good photothermal stability. The photothermal conversion efficiency (η) of the ZT/PLLA scaffold was also calculated to be 28.6%, as shown in Fig. 4d and e.

3.3. The release of H_2S and Zn^{2+}

Zinc sulfide (ZnS), as a common H_2S donor, can remain stable in a neutral environment. However, ZnS rapidly degrades and release Zn^{2+} and H_2S in acid solution, displaying pH-responsive degradation behavior. The release of H_2S at different pH (5.0, 6.2, and 7.4) was measured *via* the typical methylene blue method. The standard curves for H_2S release were recorded using Na_2S solution (Fig. 5a–c). It can be seen that the concentration of Na_2S was linearly dependent on the OD value at the absorbance of 664 nm at different pH. As shown in Fig. 5d, the amount of H_2S under neutral conditions was minimal, and the cumulative release amount in 24 h was about 35 μM. By contrast, the cumulative release amount of H_2S significantly increased at pH = 6.2 and 5.0, reaching 56.9 μM and 81.2 μM, respectively. Therefore, only acidic conditions can produce a sufficient amount of H_2S. Particularly, there is an acidic microenvironment in bacterial biofilms. Thus, the ZT/PLLA scaffold is expected to achieve biofilm microenvironment (BME)-responsive H_2S release for precise gas therapy. Zn^{2+} has been reported to play an important role in the metabolic process of bone cells.[48] Specifically, an appropriate amount of Zn^{2+} can promote osteoblast proliferation, adhesion and differentiation.[49] Therefore, the release of Zn^{2+} in PBS was detected by inductively coupled plasma-atomic emission spectrometry (ICP-AES), as presented in Fig. 5e and f, where the release of Zn^{2+} from the scaffolds was relatively high during the first 7 days and remained relatively stable in the later period. The cumulative release of Zn^{2+} within 14 days reached 0.5 mg L^{-1}.

3.4. *In vitro* antibiofilm activity

To explore the antibiofilm properties of the ZT/PLLA scaffold *in vitro*, *S. aureus* and *E. coli* were chosen as the two model bacteria. After different treatments, the biofilm was stained by crystal violet staining. The staining images of the different groups are displayed in Fig. 6a and c, respectively. Both *S. aureus* and *E. coli* basically maintained a clear and complete biofilm structure in the absence of NIR light, indicating almost no antibiofilm activity. In the NIR+ groups, the Ti_3C_2/PLLA scaffold exhibited good antibiofilm property due to its excellent photothermal ability, suggesting that hyperthermia destroyed the dense biofilm. By contrast, regardless of the application of NIR light irradiation, the single model of gas therapy (ZnS/PLLA group) possessed limited antibiofilm activity. Encouragingly, both the *S. aureus* and *E. coli* biofilms in the ZT/PLLA group under irradiation from NIR light for 20 min were significantly destroyed, which caused obvious biomass loss, displaying the best antibiofilm activity (Fig. 6a–d). These results suggest that combining hyperthermia with H_2S gas can synergistically destroy bacterial biofilms.

The spread plate method was also used to evaluate the antibacterial activities of the different scaffolds. As shown in

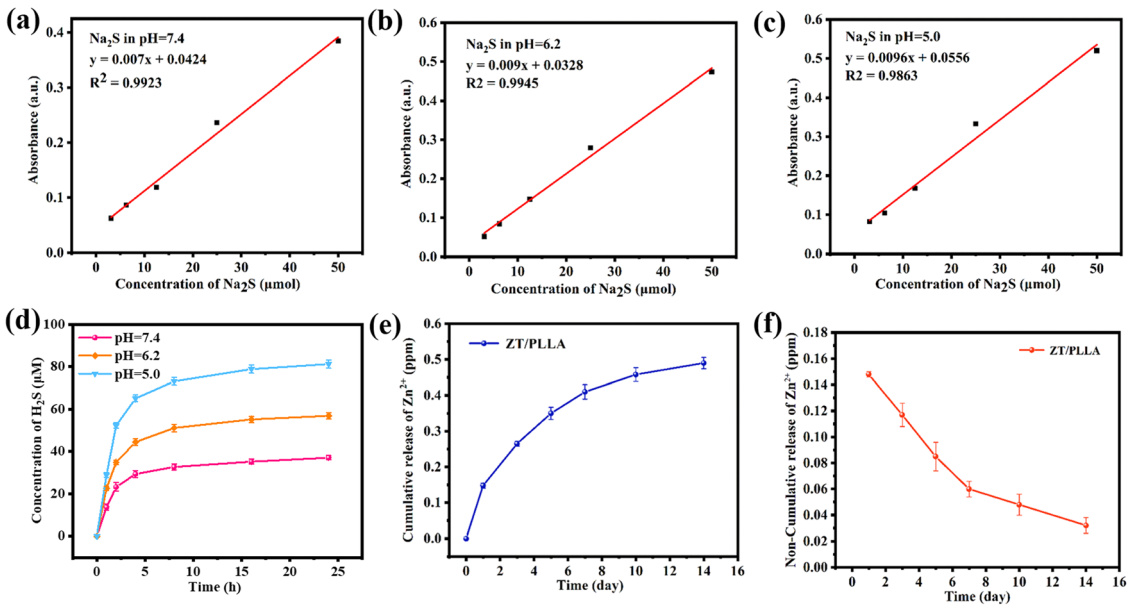

Fig. 5 (a)–(c) Na_2S standard curve at different pH. (d) Cumulative release of H_2S at different pH. Cumulative (e) and non-cumulative (f) release curves of Zn^{2+} of the ZT/PLLA scaffold in PBS.

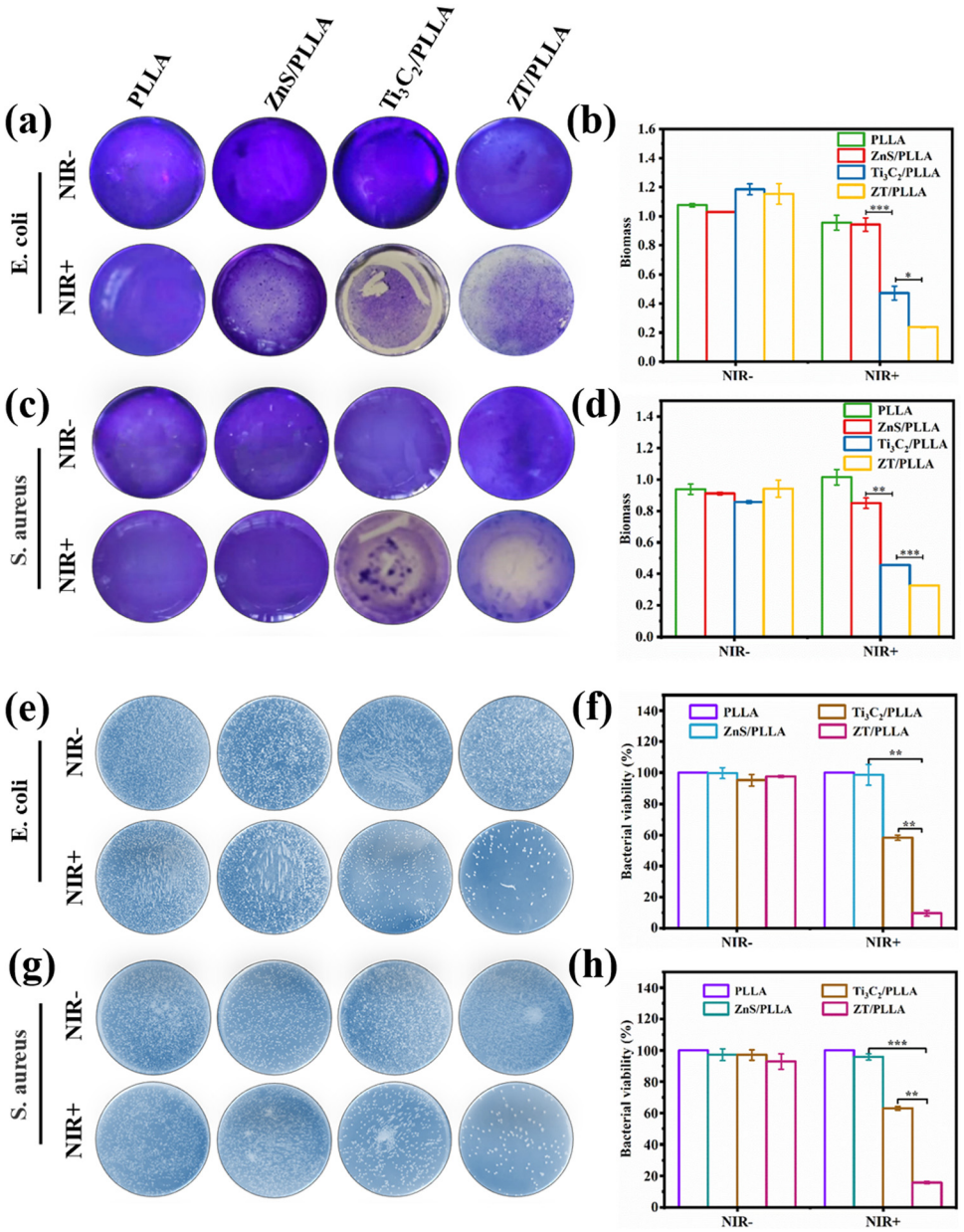

Fig. 6 *E. coli* (a) and *S. aureus* (c) biofilm crystalline violet staining after different treatments. Biofilm biomass of *E. coli* (b) and *S. aureus* (d) after different treatments. Typical photos of bacterial colonies of *E. coli* (e) and *S. aureus* (g) in different groups. Number of CFU of *E. coli* (f) and *S. aureus* (h) in different treatment groups.

Fig. 6e and g, the number of colony forming units (CFU) demonstrated the survival of intact *S. aureus* and *E. coli* bacteria in all the NIR− groups. In the NIR+ groups, the PLLA and ZnS/PLLA scaffolds also presented many colonies on the plate. However, the number of colonies was slightly reduced in the Ti_3C_2/PLLA group with NIR light irradiation due to the hyperthermia induced by Ti_3C_2. Particularly, small numbers of bacterial colonies were found in the ZT/PLLA group under irradiation from NIR light, indicating its remarkable antibacterial effects. Besides, the bacterial viability was also calculated according to the following formula: bacterial viability = $(CFU_{experimental}/CFU_{control}) \times 100\%$. As shown in Fig. 6f and h, the bacterial viability for all the groups without NIR light irradiation was over 90%. In the NIR+ groups, the PLLA and ZnS/PLLA scaffolds did not obviously reduce bacterial viability. However, the bacterial viability for the Ti_3C_2/PLLA group with NIR light irradiation fell below 60%. By contrast, the bacterial viability of *E. coli* and *S. aureus* in the ZT/PLLA group with NIR light irradiation declined to less than 10%.

In addition, the morphology of the *E. coli* biofilms was observed by SEM. All the bacterial biofilms in the NIR− groups showed an intact and undisturbed morphology (Fig. 7a). Meanwhile, the *E. coli* biofilm in the PLLA group under irradiation from NIR light irradiation was also not destroyed obviously. However, the *E. coli* biofilm in the ZnS/PLLA group after NIR light irradiation was slightly disrupted. By contrast, the *E. coli*

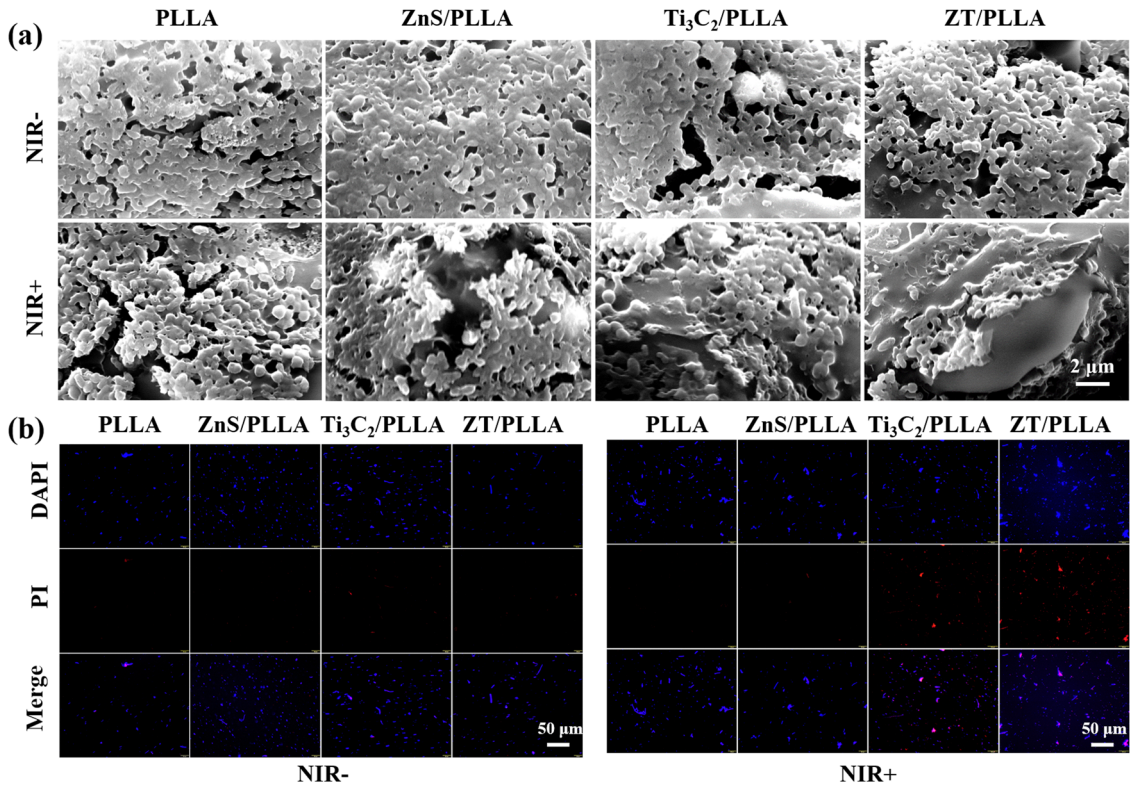

Fig. 7 (a) SEM images of *E. coli* biofilm after different treatments. (b) DAPI/PI staining images of *E. coli*.

biofilm in the Ti_3C_2/PLLA group was significantly distorted. In the case of the ZT/PLLA group with NIR+, the *E. coli* biofilm was even completely lysed. Therefore, the antibiofilm ability of the single gas treatment (ZnS/PLLA group) or hyperthermia therapy (Ti_3C_2/PLLA group) was limited, whereas the combination of gas treatment and hyperthermia therapy was effective for the elimination of the biofilm.

The bacterial viability of *E. coli* after different treatments was further evaluated through bacterial live/dead staining assays using DAPI/PI reagents. All the bacteria were stained blue by DAPI, and only dead bacteria were stained red by PI. As shown in Fig. 7b, almost no dead bacteria for all groups without NIR light irradiation were observed. In the case of the PLLA and ZnS/PLLA groups with NIR+, there were also no dead bacteria. By contrast, many dead bacteria for the Ti_3C_2/PLLA and ZT/PLLA groups with NIR light irradiation were visible, indicating excellent antibacterial ability. Meanwhile, the dead bacteria (red dots) in the ZT/PLLA group with NIR+ were the most, verifying the best antibacterial ability.

3.5. Mechanism of biofilm elimination

Extracellular DNA (eDNA) is a nucleic acid component of biofilms that exists outside the bacteria and plays an important role in bacterial adhesion and biofilm formation.[50,51] Due to the similarity between biofilm eDNA and bacterial genomic DNA (gDNA), the gDNA was extracted by the bacterial DNA extraction kit for different treatments.[52,53] The band mapping images from agarose gel electrophoresis are shown in Fig. 8a. It was observed that the expression of gDNA in the ZnS/PLLA and ZT/PLLA groups was evidently downregulated. The main reason for this was that the H_2S gas released from ZnS in an acidic microenvironment could damage the bacterial gDNA. To further elucidate the mechanism of damage to the biofilms by the scaffolds with different treatments, the eDNA from the biofilm was detected by AO staining, and the corresponding staining results are shown in Fig. 8b. Consequently, strong green fluorescence for the PLLA group with or without NIR light irradiation was observed. The intensity of the green fluorescence in the ZnS/PLLA group with or without NIR light was lower than in the PLLA groups, suggesting that the release H_2S gas can damage the eDNA of both *S. aureus* and *E. coli* biofilms. The Ti_3C_2/PLLA group with NIR+ also had some inhibitory effect on eDNA due to the hyperthermia. By contrast, almost no green fluorescence was visible in the ZT/PLLA group with NIR+, demonstrating that the integration of H_2S gas and hyperthermia had a significant ability to damage biofilm eDNA. These results are consistent with the results from the eDNA content assay (Fig. 8c and d). In conclusion, H_2S gas and hyperthermia can synergistically destroy eDNA and promote the collapse of recalcitrant biofilms.

After the destruction of the biofilm structure, the NIR light-activated hyperthermia can easily kill bacteria. Afterwards, the *O*-nitrophenyl-β-D-galactopyranoside (ONPG) assay was performed to detect the bacterial membrane permeability of *S. aureus* and *E. coli*. As shown in Fig. 8e and f, the bacterial membrane permeability of *S. aureus* and *E. coli* for all the NIR− groups did not have obvious significance, displaying no obvious cytoplasmic leakage. The Ti_3C_2/PLLA group with NIR

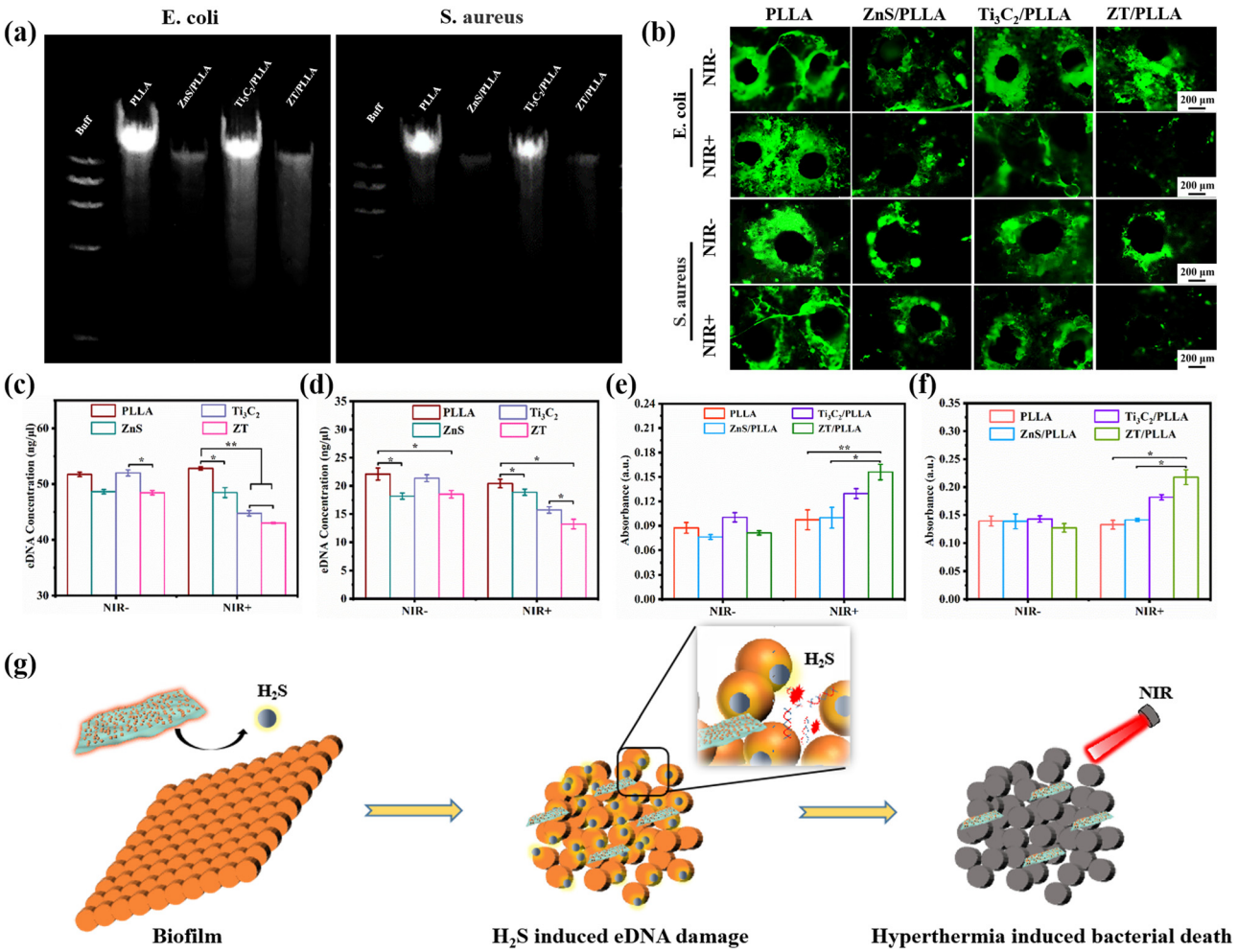

Fig. 8 (a) Agarose gel electrophoresis results of bacterial gDNA after different treatments. (b) AO staining of biofilm eDNA on the composite scaffolds. eDNA levels of *E. coli* (c) and *S. aureus* (d) biofilms after different treatments. Bacterial membrane permeability assessment by ONPG assay of *E. coli* (e) and *S. aureus* (f) after various treatments. (g) Schematic illustration of synergistic H_2S gas and hyperthermia to eliminate biofilm mechanism.

light irradiation enhanced the bacterial membrane permeability compared to the ZnS/PLLA group with NIR light irradiation, which was caused by the excellent photothermal effect induced by Ti_3C_2. In addition, the ZT/PLLA group with NIR light irradiation exhibited the highest absorbance, indicating that the synergistic effect of H_2S and hyperthermia will cause the greatest damage to the bacterial membrane. The schematic illustration in Fig. 8g reveals that H_2S gas and hyperthermia synergistically eliminate the biofilm. Firstly, the ZT nanoplatform in the composite scaffold responds to the acidic biofilm microenvironment to produce H_2S gas. Afterwards, H_2S gas can induce eDNA damage in the bacterial biofilm, and then the biofilm structure is easy to destroy by hyperthermia. After the collapse of the biofilm, the bacteria will be killed by high temperature.

3.6. Cytocompatibility and osteogenic differentiation

In addition to antibacterial properties, the cellular responses of bone scaffolds are a very important evaluation index. Firstly, the live–dead fluorescent staining of mouse bone marrow mesenchymal stem cells (mBMSCs) in different culture environments was analyzed (Fig. 9a). The number of cells increased significantly with time and almost no dead cells were found, indicating the good cytocompatibility in all groups.[54] After 5 days of culture, the cell density of the ZT/PLLA scaffold was higher than that in the other two groups. Besides, the cell proliferation of mBMSCs on days 1, 3 and 5 was measured using the CCK-8 method, as shown in Fig. 9b. There was no significant difference in the cellular activity of the samples among the groups on day 1. With an extension in the incubation time, the proliferation of mBMSCs on the ZT/PLLA scaffolds significantly increased compared to that on the PLLA and Ti_3C_2/PLLA groups. This can be attributed to the fact that the release of Zn^{2+} from the scaffolds promoted cell proliferation.

ALP is a marker of early osteogenic differentiation and is commonly used to assess the differentiation of mBMSCs.[55–57] As shown in Fig. 9c, after 7 days of culture, the ZT/PLLA group exhibited a higher level of ALP activity than the other two groups. In addition, the formation of calcium nodules in mBMSCs was observed using an alizarin red staining (ARS) assay. As displayed

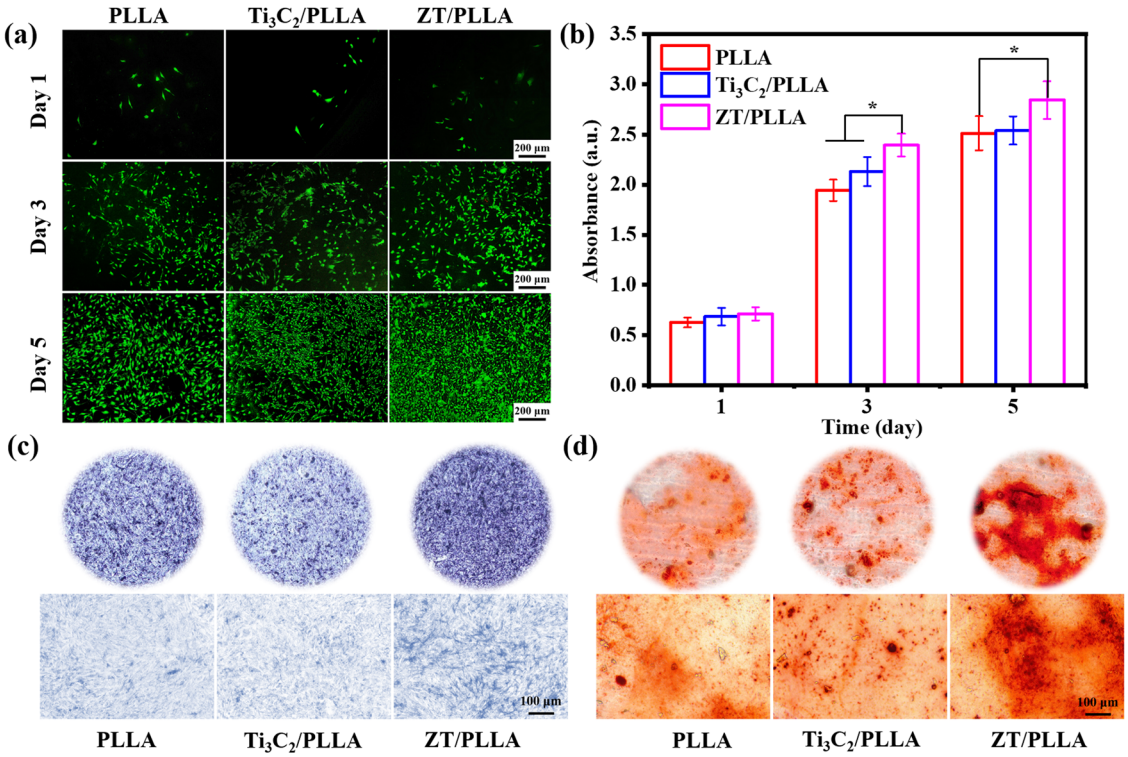

Fig. 9 Live/dead fluorescent staining (a), CCK-8 results (b), ALP staining (c) and ARS staining (d) images of mBMSCs after culturing with different scaffold extracts for different times.

in Fig. 9d, the amount of calcium nodules generated in the ZT/PLLA group was more than that in the other groups, indicating that the addition of the ZT nanoplatform evidently promoted osteogenic differentiation. The osteogenesis-promoting effect for the ZT/PLLA scaffold can be attributed to the release of Zn^{2+}. Xia *et al.*[58] obtained C-ZnO nanocarbons by carbonizing and oxidizing ZIF-8 nanostructures, thus achieving the slow release of Zn^{2+} to promote the differentiation of MSCs to osteoblasts. In addition, Yao *et al.*[59] prepared ideal ZnO coatings on the microrough surface of ZrO_2 by atomic layer deposition (ALD), which well solved the problem of ZrO_2 affecting osteoblast proliferation/differentiation due to its biologically inert surface and endowed it with certain antibacterial activity.

4. Conclusion

In conclusion, a ZnS/Ti_3C_2 (ZT) nanoplatform was constructed *via* the *in situ* growth of ZnS nanoparticles on Ti_3C_2 nanosheets, and then incorporated in PLLA to fabricate a ZT/PLLA composite scaffold using selective laser sintering technology. The results showed that the composite scaffold had excellent photothermal properties and could pH-responsively release H_2S gas. Moreover, the composite scaffold effectively eliminated biofilms, killed 90.4% of *E. coli* and 84.2% of *S. aureus* under near infrared light irradiation for 20 min *via* synergistic H_2S gas and photothermal therapies. The antibiofilm mechanism was that the produced H_2S gas can induce eDNA damage in the bacterial biofilm, and then the biofilm structure is easily destroyed by hyperthermia. After the collapse of the biofilm, the bacteria will be killed by high temperature. In addition, the composite scaffolds also promoted the proliferation and osteogenic differentiation of mouse bone marrow mesenchymal stem cells due to the release of Zn^{2+} ions. Thus, the prepared composite scaffold with good antibiofilm and osteogenic activity may provide an alternative "green therapy" for combating implant-associated infections.

Conflicts of interest

The authors declare that they have no known competing financial interests or personal relationships that could have appeared to influence the work reported in this paper.

Acknowledgements

The authors gratefully acknowledge the financial supports to this research work from the National Science Foundation of China under Grant no. 32360232, 32060222 and 82160354, and Jiangxi Provincial Natural Science Foundation under Grant no. 20232BAB216052 and 20212BAB204005.

References

1 B. Li and T. J. Webster, Bacteria antibiotic resistance: New challenges and opportunities for implant-associated orthopedic infections, *J. Orthop. Res.*, 2018, **36**(1), 22–32.

2 J. A. Inzana, E. M. Schwarz and S. L. Kates, *et al.*, Biomaterials approaches to treating implant-associated osteomyelitis, *Biomaterials*, 2016, **81**, 58–71.
3 M. Terreni, M. Taccani and M. Pregnolato, New antibiotics for multidrug-resistant bacterial strains: latest research developments and future perspectives, *Molecules*, 2021, **26**(9), 2671.
4 E. Medina and D. H. Pieper, Tackling threats and future problems of multidrug-resistant bacteria, *How to overcome the antibiotic crisis: facts, challenges, technologies and future perspectives*, 2016, pp. 3–33.
5 M. Hans, S. Mathews and F. Mücklich, *et al.*, Physicochemical properties of copper important for its antibacterial activity and development of a unified model, *Biointerphases*, 2016, **11**(1), 018902.
6 Y. Qing, L. Cheng and R. Li, *et al.*, Potential antibacterial mechanism of silver nanoparticles and the optimization of orthopedic implants by advanced modification technologies, *Int. J. Nanomed.*, 2018, 3311–3327.
7 M. I. Setyawati, X. Yuan and J. Xie, *et al.*, The influence of lysosomal stability of silver nanomaterials on their toxicity to human cells, *Biomaterials*, 2014, **35**(25), 6707–6715.
8 O. V. Morozova, Silver nanostructures: limited sensitivity of detection, toxicity and anti-inflammation effects, *Int. J. Mol. Sci.*, 2021, **22**(18), 9928.
9 P. Jiang, L. Huang and J. Wang, *et al.*, Carboxymethyl chitosan-based multifunctional hydrogels incorporated with photothermal therapy against drug-resistant bacterial wound infection, *Int. J. Biol. Macromol.*, 2022, **209**, 452–463.
10 H. J. Busscher and H. C. van der Mei, How do bacteria know they are on a surface and regulate their response to an adhering state?, *PLoS Pathog.*, 2012, **8**(1), e1002440.
11 G. F. Alotaibi and M. A. Bukhari, Factors influencing bacterial biofilm formation and development, *Am. J. Biomed. Sci. Res.*, 2021, **12**(6), 617–626.
12 W. F. Oliveira, P. M. S. Silva and R. C. S. Silva, *et al.*, Staphylococcus aureus and Staphylococcus epidermidis infections on implants, *J. Hosp. Infect.*, 2018, **98**(2 111–117.
13 A. Mondal and M. De, Exfoliation, functionalization and antibacterial activity of transition metal dichalcogenides, *Tungsten*, 2022, 1–16.
14 W. Ma, X. Chen and L. Fu, *et al.*, Ultra-efficient antibacterial system based on photodynamic therapy and CO gas therapy for synergistic antibacterial and ablation biofilms, *ACS Appl. Mater. Interfaces*, 2020, **12**(20), 22479–22491.
15 L. Yu, P. Hu and Y. Chen, Gas-generating nanoplatforms: material chemistry, multifunctionality, and gas therapy, *Adv. Mater.*, 2018, **30**(49), 1801964.
16 L. H. Fu, Z. Z. Wei and K. D. Hu, *et al.*, Hydrogen sulfide inhibits the growth of Escherichia coli through oxidative damage, *J. Microbiol.*, 2018, **56**, 238–245.
17 G. Li, H. Lei and Y. Yang, *et al.*, Titanium Sulfide Nanosheets Serve as Cascade Bioreactors for H_2S-Mediated Programmed Gas–Sonodynamic Cancer Therapy, *Adv. Sci.*, 2022, **9**(30), 2201069.
18 Z. Wang, F. Rong and Z. Li, *et al.*, Tailoring gas-releasing nanoplatforms for wound treatment: An emerging approach, *Chem. Eng. J.*, 2023, **452**, 139297.
19 H. Ci, L. Ma and X. Liu, *et al.*, Photo-excited antibacterial poly (ε-caprolactone)@ MoS_2/ZnS hybrid nanofibers, *Chem. Eng. J.*, 2022, **434**, 134764.
20 S. Alwarappan, N. Nesakumar and D. Sun, *et al.*, 2D metal carbides and nitrides (MXenes) for sensors and biosensors, *Biosens. Bioelectron.*, 2022, 113943.
21 P. Song, W. Wang and J. Li, *et al.*, Self-assembly of hydroxyapatite around Ti_3C_2 MXene/gold nanorods for efficient remotely triggered drug delivery, *Ceram. Int.*, 2022, **48**(19), 27957–27966.
22 H. Lin, X. Wang and L. Yu, *et al.*, Two-dimensional ultrathin MXene ceramic nanosheets for photothermal conversion, *Nano Lett.*, 2017, **17**(1), 384–391.
23 G. Liu, J. Zou and Q. Tang, *et al.*, Surface modified Ti_3C_2 MXene nanosheets for tumor targeting photothermal/photodynamic/chemo synergistic therapy, *ACS Appl. Mater. Interfaces*, 2017, **9**(46), 40077–40086.
24 R. Tian, J. Liu and G. Dou, *et al.*, Synergistic antibiosis with spatiotemporal controllability based on multiple-responsive hydrogel for infectious cutaneous wound healing, *Smart Mater. Med.*, 2022, **3**, 304–314.
25 X. Yao, B. Yang and J. Xu, *et al.*, Novel gas-based nanomedicines for cancer therapy, *View*, 2022, **3**(1), 20200185.
26 Y. Yang, Z. Li and P. Huang, *et al.*, Rapidly separating dissolving microneedles with sustained-release colchicine and stabilized uricase for simplified long-term gout management, *Acta Pharm. Sin. B*, 2023, **13**, 3454–3470.
27 M. Ou, C. Lin and Y. Wang, *et al.*, Heterojunction engineered bioactive chlorella for cascade promoted cancer therapy, *J. Controlled Release*, 2022, **345**, 755–769.
28 C. Lin, C. Huang and Z. Shi, *et al.*, Biodegradable calcium sulfide-based nanomodulators for H2S-boosted Ca2+-involved synergistic cascade cancer therapy, *Acta Pharm. Sin. B*, 2022, **12**(12), 4472–4485.
29 M. Yu, J. Yu and Y. Yi, *et al.*, Oxidative stress-amplified nanomedicine for intensified ferroptosis-apoptosis combined tumor therapy, *J. Controlled Release*, 2022, **347**, 104–114.
30 G. Qian, L. Zhang and G. Wang, *et al.*, 3D printed Zn-doped mesoporous silica-incorporated poly-L-lactic acid scaffolds for bone repair, *Int. J. Bioprint.*, 2021, **7**(2), 92–103.
31 W. Xiong, L. Yuan and J. Huang, *et al.*, Direct osteogenesis and immunomodulation dual function via sustained release of naringin in the polymer scaffold, *J. Mater. Chem. B*, 2023, **11**(45), 10896–10907.
32 Y. Yu, K. Liu and Z. Wen, *et al.*, Double-edged effects and mechanisms of Zn^{2+} microenvironments on osteogenic activity of BMSCs: Osteogenic differentiation or apoptosis, *RSC Adv.*, 2020, **10**(25), 14915–14927.
33 G. Qian, Y. Mao and Y. Shuai, *et al.*, Enhancing bone scaffold interfacial reinforcement through in situ growth of metal–organic frameworks (MOFs) on strontium carbonate: Achieving high strength and osteoimmunomodulation, *J. Colloid Interface Sci.*, 2024, **655**, 43–57.

34 G. Qian, L. Zhang and Y. Shuai, *et al.*, 3D-printed $CuFe_2O_4$-MXene/PLLA antibacterial tracheal scaffold against implantation-associated infection, *Appl. Surf. Sci.*, 2023, **614**, 156108.
35 L. Wang, J. Cao and Y. H. Zhou, *et al.*, Design and characterization of monolayer Ti_3C_2 MXene/$NiCo_2O_4$ nanocones hybrid architecture for asymmetric supercapacitors, *J. Electroanal. Chem.*, 2022, **923**, 116787.
36 G. Qian, L. Zhang and X. Liu, *et al.*, Silver-doped bioglass modified scaffolds: A sustained antibacterial efficacy, *Mater. Sci. Eng., C*, 2021, **129**, 112425.
37 G. Qian, T. Wen and S. Shuai, *et al.*, Photothermal and photodynamic effects of g-C_3N_4 nanosheet/Bi_2S_3 nanorod composites with antibacterial activity for tracheal injury repair, *ACS Appl. Nano Mater.*, 2022, **5**(11), 16528–16543.
38 G. Qian, J. Wang and L. Yang, *et al.*, A pH-responsive CaO_2@ZIF-67 system endows a scaffold with chemodynamic therapy properties, *J. Mater. Sci.*, 2023, 1–15.
39 D. K. Roper, W. Ahn and M. Hoepfner, Microscale heat transfer transduced by surface plasmon resonant gold nanoparticles, *J. Phys. Chem. C*, 2007, **111**(9), 3636–3641.
40 A. Feng, Y. Yu and F. Jiang, *et al.*, Fabrication and thermal stability of NH_4HF_2-etched Ti_3C_2 MXene, *Ceram. Int.*, 2017, **43**(8), 6322–6328.
41 J. Liu, T. Xin and Z. Yang, *et al.*, Bi_2S_3/ZnS heterostructures for H_2S sensing in the dark: the synergy of increased surface-adsorbed oxygen and charge transfer, *Inorg. Chem. Front.*, 2022, **9**(19), 4921–4929.
42 S. Pina, J. M. Oliveira and R. L. Reis, Natural-based nanocomposites for bone tissue engineering and regenerative medicine: A review, *Adv. Mater.*, 2015, **27**(7), 1143–1169.
43 S. Torgbo and P. Sukyai, Bacterial cellulose-based scaffold materials for bone tissue engineering, *Appl. Mater. Today*, 2018, **11**, 34–49.
44 Y. Wang, Q. Zhang and Y. Zhou, *et al.*, Current progress of key technology of porous bone tissue scaffold manufacturing using selective laser sintering rapid prototyping (SLS), Proceedings of the 4th International Convention on Rehabilitation Engineering & Ass Technology, 2010, pp. 1-5.
45 J. Zan, Y. Shuai and J. Zhang, *et al.*, Hyaluronic acid encapsulated silver metal organic framework for the construction of a slow-controlled bifunctional nanostructure: Antibacterial and anti-inflammatory in intrauterine adhesion repair, *Int. J. Biol. Macromol.*, 2023, 123361.
46 C. Gao, X. Yao and Y. Deng, *et al.*, Laser-beam powder bed fusion followed by annealing with stress: A promising route for magnetostrictive improvement of polycrystalline Fe81Ga19 alloys, *Addit. Manuf.*, 2023, **68**, 103516.
47 H. Li, X. Song and B. Li, *et al.*, Carbon nanotube-reinforced mesoporous hydroxyapatite composites with excellent mechanical and biological properties for bone replacement material application, *Mater. Sci. Eng., C*, 2017, **77**, 1078–1087.
48 B. Wang, M. Yang and L. Liu, *et al.*, Osteogenic potential of Zn 2 + -passivated carbon dots for bone regeneration in vivo, *Biomater. Sci.*, 2019, **7**(12), 5414–5423.
49 Y. Yu, K. Liu and Z. Wen, *et al.*, Double-edged effects and mechanisms of Zn 2+ microenvironments on osteogenic activity of BMSCs: Osteogenic differentiation or apoptosis, *RSC Adv.*, 2020, **10**(25), 14915–14927.
50 H. Panlilio and C. V. Rice, The role of extracellular DNA in the formation, architecture, stability, and treatment of bacterial biofilms, *Biotechnol. Bioeng.*, 2021, **118**(6), 2129–2141.
51 D. Campoccia, L. Montanaro and C. R. Arciola, Extracellular DNA (eDNA). A major ubiquitous element of the bacterial biofilm architecture, *Int. J. Mol. Sci.*, 2021, **22**(16), 9100.
52 V. Svarcova, K. Zdenkova and M. Sulakova, *et al.*, Contribution to determination of extracellular DNA origin in the biofilm matrix, *J. Basic Microbiol.*, 2021, **61**(7), 652–661.
53 P. K. Sahu, P. S. Iyer and A. M. Oak, *et al.*, Characterization of eDNA from the clinical strain Acinetobacter baumannii AIIMS 7 and its role in biofilm formation, *Sci. World J.*, 2012, **2012**, 973436.
54 T. Su, A. Zheng and L. Cao, *et al.*, Adhesion-enhancing coating embedded with osteogenesis-promoting PDA/HA nanoparticles for peri-implant soft tissue sealing and osseointegration, *Bio-Des. Manuf.*, 2022, **5**(2), 233–248.
55 R. P. Pirraco, R. L. Reis and A. P. Marques, Effect of monocytes/macrophages on the early osteogenic differentiation of hBMSCs, *J. Tissue Eng. Regener. Med.*, 2013, **7**(5), 392–400.
56 Z. Gong and F. H. Wezeman, Inhibitory effect of alcohol on osteogenic differentiation in human bone marrow–derived mesenchymal stem cells, *Alcohol.: Clin. & Exp. Res.*, 2004, **28**(3), 468–479.
57 X. Sun, X. Zhang and X. Jiao, *et al.*, Injectable bioactive polymethyl methacrylate–hydrogel hybrid bone cement loaded with BMP-2 to improve osteogenesis for percutaneous vertebroplasty and kyphoplasty, *Bio-Des. Manuf.*, 2022, **5**(2), 318–332.
58 Y. Xia, X. Fan and H. Yang, *et al.*, ZnO/Nanocarbons-Modified Fibrous Scaffolds for Stem Cell-Based Osteogenic Differentiation, *Small*, 2020, **16**(38), 2003010.
59 L. Yao, X. Wu and S. Wu, *et al.*, Atomic layer deposition of zinc oxide on microrough zirconia to enhance osteogenesis and antibiosis, *Ceram. Int.*, 2019, **45**(18), 24757–24767.

